A Comparative Study for Control of Semi-Automatic Robotic-assisted Ultrasound System in Spine Surgery

Ayoob Davoodi, Ruixuan Li, Yuyu Cai, Kenan Niu, Gianni Borghesan, and Emmanuel Vander Poorten

***Abstract*— Ultrasound (US) imaging has been widely applied in different clinical scenarios thanks to its low-cost and non-radiative nature. Recently, robotic US has increasingly become a technology to produce 3D US reconstructions for navigation during surgical interventions. It is considered a promising technology to address variable skills among human sonographers. Dedicated control strategies are needed to ensure high-quality US reconstructions that are comparable or superior to those generated by human experts. The robot controller ought to establish human-like scanning maneuvers while maintaining tight skin contact and ensuring essential safety. In essence, this means that at all times, the robot should avoid applying excessive force on the patient. Therefore, a comparative study on the admittance-based controllers was conducted while a semi-automatic path planning approach was used to realize automatic US scanning. The developed system was validated by scanning a synthetic phantom, compared with position and admittance control. The robotic US system with the proposed control applied a force lower than 3.83 ± 0.31 N while ensuring continuous US imaging. By defining the successful rate as the US image has more than 90% of soft tissue (i.e., ligament) length, the velocity-based admittance controller has more than 80% successful US imaging. Such an approach could contribute to the further development and uptake of robotic US systems in spine surgery and possibly beyond.**

Keywords: admittance control, ultrasound reconstruction, robot-assisted system

I. INTRODUCTION

Robotic-assisted Ultrasound (US) technology has been increasingly utilized in orthopedic surgery to improve surgical efficiency [1]. When used for 3D US reconstruction, it can provide the clinician with a radiation-free tool to visualise some anatomic structures in real-time and guide the movement of surgical instruments [2, 3, 4]. Robotic US can be used for pre-operative diagnosis, intraoperative navigation, or post-operative treatment assessment. However, it is well known that the quality of the reconstruction is highly dependent on the adopted scanning strategy [5]. Aside from the right scanning strategy, the system should also be able to execute the scan path reliably.

Prior research that searches for the optimal scanning approach indicated that it is essential to maintain good contact between the US probe and the patient by extracting the projection of normal force from the measured contact force and trying to keep constant normal force [6, 7, 8, 9, 10, 11]. In [6], a mechanical model with a spring-compliant controller was developed to find the rotation of the US probe around a normal axis to keep a constant normal force. The measured force was fed into a model that then estimated the direction normal to the surface. After that, a position controller was used to rotate the probe to align it to the estimated normal vector. To improve the scanning performance, Jiang *et al.* continued and implemented a US confidence map to adjust the in-plane orientation of the probe [7]. The work suggested a quality improvement of the US-generated images with $3.2 \pm 1.7^\circ$ less normal vector rotation error compared to six human operators' manual US scanning. Similarly, an admittance model based robotic-assisted US system was proposed to maintain the US probe at an optimal angle, which is normal to the tissue surface, and ensure stable contact with minimal tissue deformation in breast volume scanners [8, 9]. Victorova *et al.* introduced a framework using a 3D US reconstruction for qualitatively scoliosis assessment [10] using decoupled position control and normal force control. Jia et al. also developed a dynamic program for US image segmentation. It has already achieved good results with an

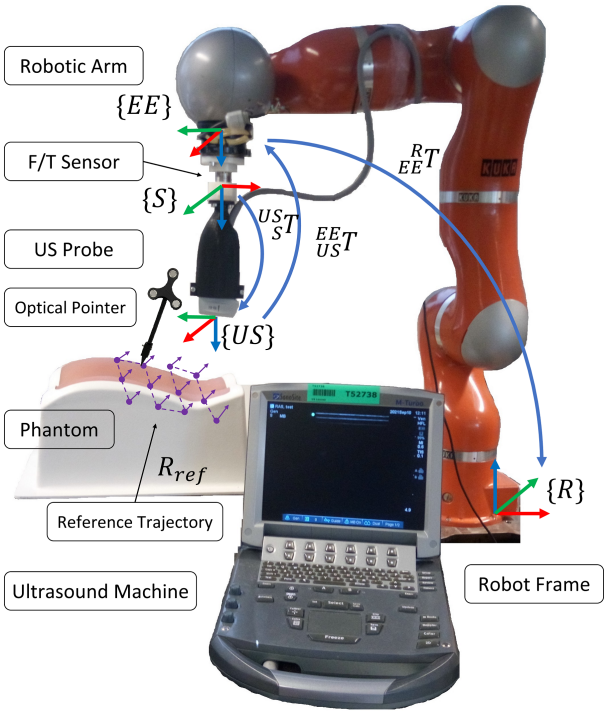

Fig. 1: The experimental setup with the lumbar phantom.

A. Davoodi, R. Li, Y Cai, G. Borghesan, and E. Vander Poorten are with the Department of Mechanical Engineering, KU Leuven, Belgium (email: ayoob.davoodi@kuleuven.be)

K. Niu is with the Department of Robotics and Mechatronics, University of Twente, Enschede, The Netherlands

This project has received funding from the European Union's Horizon 2020 research and innovation programme under grant agreement No 101016985 (FAROS) and Flemish Research Foundation (FWO) under grant agreement NO.G0A1420N (Radar-spine) and NO.1S36322N (Harmony).

average accuracy of less than 0.3 mm [11].

The aforementioned research focused on optimizing the contact force while ensuring better US image quality. Nevertheless, the impact of US image feedback is also crucial for robot-assisted US scanning. In [12], a visual servoing for needle tracking was done on the flat phantom to keep a constant 2 N force in the normal direction. However, that control approach was not applicable to general clinical scenarios with curved surfaces. Huang *et al.* developed a robotic US system based on a depth camera to find the normal vector of the scanning surface[13]. However, their control strategy cannot regulate the force around a desired value. The US probe was moved along the normal vector direction when the applied force was outside the range the 1 to 8 N.

Thus, to address this issue, we investigated control strategies in which admittance-based control is integrated and feedback with real-time force measurement. With this approach, we maintain constant contact with both deformable and moving surfaces during US scanning. The present work aims to comprehensively compare several control strategies with a semi-automatic robotic US system. In particular, our contributions are as follows:

- By using a hybrid admittance control, the US probe follows the desired trajectory and remains in contact with the patient's skin with a compliant behavior.
- Comparing several admittance-based control strategies to achieve the highest performance in the US scanning. The comparison is designed to cope with a US scanning quality assessment and performance evaluation.

This paper is organized as follows. Section II describes the employed methods including a system overview and explanations on: path planning, control strategies, experiment design, and evaluation criteria. Section III reports the results of the semi-automatic scanning experiments conducted on an artificial phantom. Section IV discusses the proposed system and concludes at the end.

II. METHODS

An envisioned semi-automatic workflow for reconstructing a 3D spine surface model from US imaging is depicted in Fig. 2. In this approach, the robot follows a trajectory taught by the clinician. Hereto, the clinician places an optical pointer at several points on the patient's skin. These points then span the area to be scanned by the US robot. The points are stored and used to compute an S-shape trajectory subsequently. After that, the robot follows the generated path while regulating a constant interaction force along a direction normal to the tissue. During the scanning, the poses of the robot end effector and US images are recorded simultaneously for 3D US reconstruction. The contours of the bone are segmented from 2D images. Subsequently, the segmented 2D points can thus be converted into 3D points by taking US image calibration [14], 6 DoF pose information of the end-effector. Once this procedure is finished, the pixels in 2D US images are transformed into 3D space in the robot frame. Finally, the computed pointclouds are rendered as a 3D model to show the anatomical features of the lumbar model. Each block of Fig.2 is explained in the following.

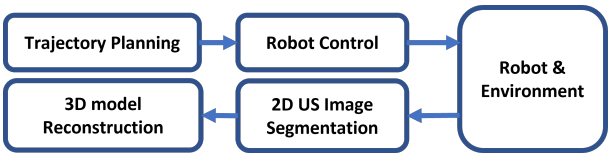

Fig. 2: Workflow of semi-automatic US scanning for 3D US reconstruction.

A. Trajectory Planning

Generating a scanning path that is normal to the skin surface is regarded as a reasonable way to increase the US reflection of the bony structures and decrease the attenuation of the US beam. Generating the scanning path highly depends on the clinician's skill and the region of interest shape. To have a precise scanning path, an optical camera system is used to obtain the scanning reference trajectory. The predefined scanning path was generated following an S-shape with a constant distance of 20 mm between subsequent on-surface selected points(shown in Fig.3B). The purple dashed lines were the reference path $R_{ref} = [\mathbf{p_{ref}}, \theta_{\mathbf{ref}}] \in \mathbb{R}^6$ generated from the recorded points. Each point was connected to the next one by a straight line while the robots followed a trapezoidal velocity profile of $4mm/s$ to reach the new point. Because of using an external optical camera, a camera-to-robot calibration was performed to estimate the camera-to-robot transformation (${}^R_C T$) according to the previous study [15]. By obtaining the camera-to-robot calibration, the poses of the recorded point were converted from the camera frame $\{C\}$ to the robot frame $\{R\}$; The scanning trajectory was obtained with an optical pointer from the skin surface.

B. Robot Control Schemes

Different semi-automatic robotic scanning controllers are implemented. The transformation is presented in the world frame (i.e., the robot-based frame). The force/torque (F/T) sensor measuring data, which is recorded in the sensor frame, is transformed to the probe's end effector frame using T^S_{EE}. Hereinafter, the control equations are described in the robot base frame $\{R\}$ unless otherwise mentioned.

To precisely guide the US probe across the surface and maintain a constant normal contact force, an admittance-based controller is depicted Fig.3; where the desired pose $R_d = [\mathbf{p_d}, \theta_{\mathbf{d}}] \in \mathbb{R}^6$ represents the position and Euler angles of the US probe frame $\{US\}$. To have smooth and continuous imaging, the US probe should be aligned to the surface's normal vector and apply a constant force on the skin surface. Therefore, the desired wrench vector $w_d = [0,0,f_z,0,0,0] \in \mathbb{R}^6$ in the probe frame $\{US\}$ is a constant force in the z-direction. The admittance control law converts the wrench error $w_e = w_d - w_m = [\mathbf{f}_e, \tau_e] \in \mathbb{R}^6$ to a deviation of the desired pose $R_e = [\mathbf{p_e}, \theta_{\mathbf{e}}] \in \mathbb{R}^6$, expressed in the robot frame $\{R\}$. Here $w_m \in \mathbb{R}^6$ and $\mathbf{p_e} \in \mathbb{R}^3$ and $\theta_{\mathbf{e}} \in \mathbb{R}^3$ are the measured wrench, position deviation, and orientation

deviation, respectively. The proposed control approach has distinctive compliant behaviour defined by a dynamic model for each DoF, which is selected by the Selection matrix $\mathbf{S} = diag([0,0,1,0,0,0])$. Reaching a constant force and following the surface fluctuation on the skin urges to use of a velocity-based compliant behaviour for the force error along the probe Z-axis(Fc in Fig.3A):

$$F_{ch}: \quad \dot{p}_{e_z} = c_z f_{e_z} \tag{1}$$

Where $\dot{p}_{e_z}$ and c_z are the velocity of position deviation along the Z-axis and the compliance coefficient, respectively; from now on, we call it the velocity-based admittance controller. A second-order dynamic model is used for the other axes. This leads to the behaviour similar to a physical mass-spring-damper element (G_c in Fig.3A).

$$G_{c2}: \begin{cases} \mathbf{M}\ddot{\mathbf{p}}_{\mathbf{e_{x,y}}} + \mathbf{B}\dot{\mathbf{p}}_{\mathbf{e_{x,y}}} + \mathbf{K}\mathbf{p}_{\mathbf{e_{x,y}}} = \mathbf{f}_{e_{x,y}} \\ \mathbf{I}\ddot{\theta}_{\mathbf{e}} + \mathbf{V}\dot{\theta}_e + \mathbf{C}\theta_{\mathbf{e}} = \tau_e \end{cases} \tag{2}$$

Where $\dot{\mathbf{p}}_{\mathbf{e_{x,y}}} \in \mathbb{R}^2, \dot{\theta}_e \in \mathbb{R}^3$ and $\ddot{\mathbf{p}}_{\mathbf{e_{x,y}}} \in \mathbb{R}^2, \ddot{\theta}_e \in \mathbb{R}^3$ are the first and the second derivatives of the position and orientation deviations. $\mathbf{M}^{2\times2}(kg)$, $\mathbf{B}^{2\times2}(\frac{N}{m/s})$, $\mathbf{K}^{2\times2}(\frac{N}{m})$, $\mathbf{I}^{3\times3}(kgm^2)$, $\mathbf{V}^{3\times3}(\frac{N.m}{rad/s})$, $\mathbf{C}^{3\times3}(\frac{N.m}{rad})$ correspond to the mass, damper, linear stiffness, moment of inertia, viscosity, and angular stiffness matrices, respectively. The output of the compliance control is fed to the activation functions A_g,A_f, which enables/disables the compliant behaviour in the selected degree of freedom of the US probe, and its value could be 1 or 0. The desired pose of the US probe R_d is the summation of reference trajectory R_{ref} and pose deviation R_e as follows:

$$R_d = R_{ref} + R_e \tag{3}$$

The computed desired pose is fed to the Inverse Kinematic block to find the corresponding desired joint angles q_d. Based on the q_d that is sent to the robot's controller, the required torques for each joint are calculated internally by the robot driver.

Instead of having a velocity-based relation for the force along the Z-axis Eq. 1, a first or second-order dynamic model could also produce a desired compliant behavior while interacting with the environment and following the surface fluctuations. Therefore two different types of compliant models are considered:

$$F_{c2}: \quad m\ddot{p}_{e_z} + b\dot{p}_{e_z} + kp_{e_z} = f_{e_z} \tag{4}$$

$$F_{c1}: \quad b\dot{p}_{e_z} + kp_{e_z} = f_{e_z} \tag{5}$$

where m, b, k are mass, damper, and linear stiffness coefficients, respectively. Changing the dynamic model of the admittance controller leads to different interaction responses to the environment [16]; therefore, we have considered a first-order dynamic model by setting $\mathbf{M}, \mathbf{I}$ as zero in equation Eq.2:

$$G_{c1}: \begin{cases} \mathbf{B}\dot{p}_{e_{x,y}} + \mathbf{K}p_{e_{x,y}} = \mathbf{f}_{e_{x,y}} \\ \mathbf{V}\dot{\theta}_{\mathbf{e}} + \mathbf{C}\theta_e = \tau_e \end{cases} \tag{6}$$

Selecting the activation function as zero ($Af = 0$ or $Ag = 0$) turns off the complaint behavior of the control for the selected axis, which means the US probe follows the reference trajectory R_{ref} without considering the force interaction; thus, the control mode becomes the position control only.

C. Experimental Design

The experimental setup is shown in Fig. 1. The robotic US system consists of a lightweight KUKA LWR (KUKA Roboter GmbH, Augsburg, Germany) and an US imaging system. A linear B-mode US probe was attached to the robot end-effector using a 3D-printed housing. The US images were acquired with the US machine (Sonosite, FUJIFILM, USA) and recorded at 30 HZ using the frame grabber (Epiphan Systems Inc. Palo Alto, Canada). A 6 DoF F/T sensor (Nano25, ATI Industrial Automation Inc.) was assembled on the robotic end effector to measure the interaction forces/torque between the US probe and the tissue surface. A lumbar phantom (Model 034, CIRS, USA) was employed for experimental reconstruction and validation. Besides, an optical tracking system (FusionTrack 500, Atracsys, Switzerland) was integrated and operated at 50 Hz. The optical camera played the role of localization and mapping system. The robotic arm is controlled via KUKA's Fast Robot Interface (FRI), and the synthesized control system is equipped with a real-time task execution environment. OROCOS RTT allows direct control of robot functionalities through the Robot Operating System (ROS) framework. In addition, a PC workstation with an Nvidia P2000 GPU was used for US image segmentation and visualization with a deep learning network.

After generating the scanning path, the optical marker was removed from the phantom. The US gel was applied to the phantom over the scanning area. Subsequently, the robot explored the area employing various control strategies. The study involved a comparison of 9 distinct sets of dynamical models referring to Tab. I. Here, F_{ci} represented the dynamical model controlling the motion along the Z-axis of the US probe, while G_{cj} pertained to the dynamical model governing the other 5 degrees of freedom.

TABLE I: Dynamical model sets for US scanning;

	$G_{c2} = m\ddot{x} + b\dot{x} + kx$	$G_{c1} = b\dot{x} + kx$	$G_{c0} = 0$
$F_{c2} = m\ddot{x} + b\dot{x} + kx$	✓	✓	✓
$F_{c1} = b\dot{x} + kx$	✓	✓	✓
$F_{ch} = c\dot{x}$	✓	✓	✓

To ensure high-quality images in the US scans, it is crucial that the recorded trajectory points were aligned perpendicular to and in contact with the surface being scanned. Otherwise, the increasing deviation from the normal vector would cause the US waves to be scattered away rather than reflected back to the probe in the receiving image [17]. The study also investigated the effects of incorrect trajectory point selection. Apart from the initially selected trajectory (on the surface), two additional trajectories were generated by adding d mm

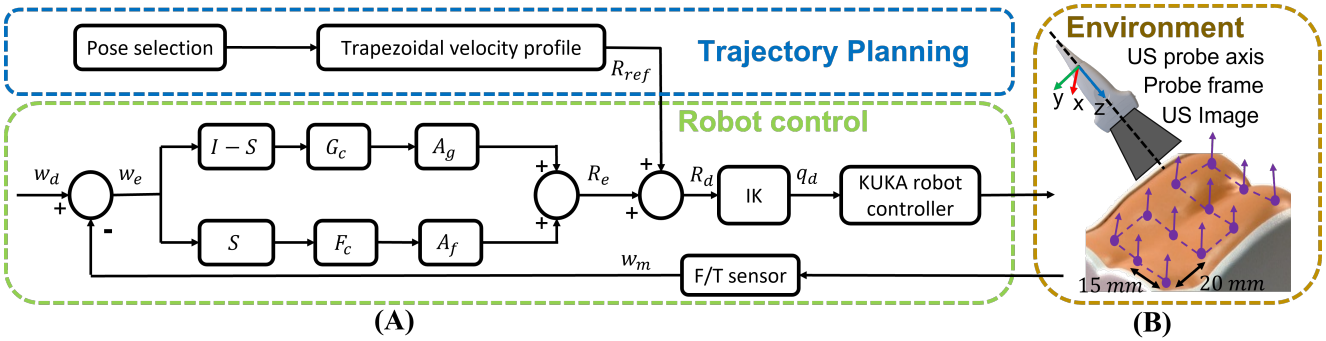

Fig. 3: A) Admittance-Based Control Block Diagram. B) the S-shaped trajectory defined on the region of interest.

along the normal vector programmatically: one moving 2 mm up along the normal vector ("Above" the surface) and the other moving 2 mm down along the normal vector ("Below" the surface). Each control strategy was executed with these three trajectories, and the corresponding US images and robot data were recorded, stored, and analyzed.

Regarding the control parameter selection, higher stiffness values are preferred to limit the steady-state error. However, a higher stiffness also decreases the actuation speed, such that the probe cannot quickly follow fluctuations of the skin surface. Thus, a stiffness value similar to the experimental phantom is chosen; during US scanning, k and C are set to 1 N/mm and 5 Nm/rad, respectively. The other second-order dynamic model parameters are selected to have a 20 rad/s bandwidth, resulting in a fast response time for the following surface fluctuations and also canceling measurement noise in the F/T sensor. The dynamical model parameters are summarized in Tab. II.

TABLE II: Dynamical model parameters; which I_n is the identity matrix of size n.

model	parameters
F_{c2}	$k = 1(\frac{N}{mm}), b = 0.7(\frac{N}{mm/s}), m = 2.5(kg)$
F_{c1}	$k = 1\frac{N}{m}, b = 0.5\frac{N}{mm/s}$
F_{ch}	$c_z = 0.5(\frac{mm/s}{N})$
G_{c2}	$\mathbf{K} = 1I_2(\frac{N}{mm})$, $\mathbf{B} = 0.7I_2(\frac{N}{mm/s})$, $\mathbf{M} = 2.5I_2(kg)$ $\mathbf{C} = 5I_3(\frac{N.m}{rad})$, $\mathbf{V} = 0.35I_3(\frac{N.m}{rad/s})$, $\mathbf{I} = 0.0125I_3(kgm^2)$
G_{c1}	$\mathbf{K} = 1I_2(\frac{N}{mm})$ $\mathbf{B} = 0.5I_2(\frac{N}{mm/s})$ $\mathbf{C} = 5I_3(\frac{N.m}{rad})$, $\mathbf{V} = 0.25I_3(\frac{N.m}{rad/s})$,

D. Evaluation

Several experiments with the proposed control methods were carried out for quantitative and qualitative measurement of the lumbar phantom.

1) Scanning Performence: The performance of the admittance-based controllers was assessed by comparing the normal contact force for different control methods. In this work, we have done semi-automatic scanning while the desired normal force was set to 4 N. The US scanning protocol for all three reference trajectories involved scanning the surface of interest of the phantom and generating the corresponding pointclouds. The robotic arms moved the US probe along the path while simultaneously capturing the US images, robot end-effector poses, and measured forces.

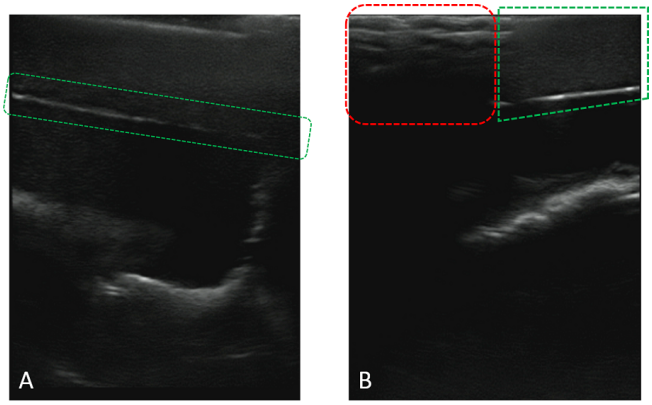

Fig. 4: Examples of the US image with A) good probe-skin contact with a continuous ligament surface and B) bad probe-skin contact with missing ligament reflection (red).

2) 2D Image Quality: To quantitatively assess the stability and validity of the control methods, image segmentation was conducted on the acquired US images to detect soft tissues (i.e., ligament), as illustrated in Fig. 4A. If the US probe is in contact with the phantom surface, the ligament can be detected (green zone in the Fig. 4A); otherwise, lousy probe-skin contact would lead to missing ligament reflection (red zone in the Fig. 4B). A deep-learning network, U-Net [18], was employed to process the recorded US images to assess the image quality. The network was trained with 1000 images collected from the same phantom. The training dataset was manually collected and labeled by the operator before validation. The model was trained for 10 epochs with a learning rate of $1e-4$. The batch size was set to 2. Subsequently, the model was used for validation. The ligament was segmented as the target objective; its contour was extracted by Canny detection. The visibility of the ligament in the US image sequence was defined as the evaluation indexes. Meanwhile, an index L_{90} was employed to present the percentage of good images with a ligament longer than 90% of the full length, which is 240 pixels.

3) 3D US Reconstruction: The US reconstruction aimed to reconstruct the 3D surface meshes from the anatomic features in the 2D US images for hard tissue (i.e., bone). A U-Net-based program segmented the US images and extracted the edges of different anatomy at the pixel level, as described in [19]. After segmentation, the images were processed with thresholding and a morphological operator. The Canny edge detection extracts the bone contours from the processed images. Subsequently, the segmented 2D US images were reconstructed with the proposed approaches. Each pixel was represented in the robot base frame. Since the US probe moves with a constant forward velocity of 4 mm/s along the path, the number of reconstructed pointclouds is used as a verification index for the 3D US reconstruction.

III. EXPERIMENTAL RESULTS

Following the completion of the experimental protocol on the spine phantom, the obtained experimental results from the US scanning performed "On" the surface of the phantom are presented in Tab. III for different control approaches. The scan of two additional experimental conditions, namely "Above" and "Below" the surface, is displayed in Fig. 6, showing the correlation and outcomes of the evaluation metrics with respect to depth along the probe Z axis.

A. Results of Scanning Performance

To evaluate the stability of the controllers, we analyzed the mean, standard deviation (Std. Dev.), maximum, and minimum values of the normal force. Fig.6A demonstrates the mean contact force variations with respect to depth. When using velocity-based control F_{ch} for the Z-axis, a constant force was achieved, while employing first or second dynamic models F_{c1}, F_{c2} resulted in a descending force. Table Tab. III presents a comparison of the mean contact force obtained from different control methods. Position control (Exp. 10) yielded a mean contact force of 2.13 ± 1.55 N, while admittance control (Exp. 1) achieved 2.39 ± 1.13 N. The proposed admittance control (Exp. 3) provides a stable contact force of 3.82 ± 0.31 N, with minor deviation in comparison to position and admittance control. In particular, the proposed admittance control approach demonstrated a reduced range of contact force variation of 2.62 N. Fig. 5 illustrates an example of the contact forces generated by the three control methods, including position control (Exp. 10), admittance control (Exp. 1), and velocity admittance control (Exp. 3). clearly showing the stability of the contact force with the proposed control method.

B. Results of 2D Image Quality

The image quality assessment relies on the coverage rate defined by ligament length, which was evaluated in pixels as a measurement. Several metrics are computed for each experiment, including the mean, standard deviation, and coverage ratio L_{90} (number of images with 90% of the ligament length). The graph in Fig. 6B displays the mean coverage as a function of depth. When utilizing velocity-based control along the Z-axis, a consistent ligament length

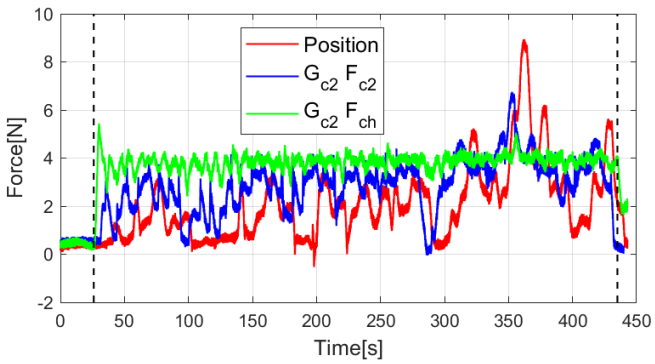

Fig. 5: An example of the contact force measurement along the probe's Z axis with the three proposed control strategies: position control (Exp. 10), admittance control (Exp. 1), and velocity admittance control (Exp. 3).

is achieved. However, employing the first or second dynamic models shows a declining trend, as moving from "Below" to "Above" reduces the contact area of the US probe with the phantom surface.

The summarized results of scanning "On" the surface are presented in Tab. III. Using the position control method (Exp. 10), the segmented ligament's length is 136.64 ± 81.66 units. With the velocity-admittance control method (Exp. 3), the average segmented ligament length is 182.1 ± 70.68 units, while 196.53 ± 57.97 units for the admittance control method (Exp. 2). The best-segmented ligament length, with a higher L_{90}, is achieved using the control method (Exp. 6: G_{c2} and F_{ch}), with an increase of $+73\%$ with respect to position control.

C. Results of 3D US Reconstruction

The evaluation of 3D reconstruction results from US scanning relies on the number of pointclouds. Implementing velocity-based control for the Z-axis leads to a higher pointclouds count compared to using a first or second-order dynamical model. This is due to applying uniform compression across the scanning area, as shown in Fig.6C. The summarized results of 3D reconstruction "On" the surface are presented in Tab. III. Regarding the 3D reconstruction process, the position control method (Exp. 10) produces a model containing 1.65×10^6 points. In contrast, the velocity admittance control (Exp. 3) achieves a higher count of 1.93×10^6 points. Examples of the 3D reconstructed model using these different control methods are demonstrated in Fig. 7, where the green line shows the top view of the scan area. When the position control is used, the lower amount of top surface is reconstructed compared to the admittance controller and velocity admittance control. The gap between the US probe and phantom skin is filled in with enough US gel. Although the contact force goes to zero, the bone contour can still be monitored in the 2D images and reconstructed into 3D space.

TABLE III: Experimental results of contact force, the length of segmented ligament, and 3D reconstructed pointclouds for "On" the surface experiment.

Exp.	Control Method		Force [N]					Segmented ligament length [pixel]			3D US reconstruction
			Mean	Std. Dev.	Min	Max	Range	Mean	Std. Dev.	L_{90}	Num of point [$\times 10^6$]
1	$G_{c2} = m\ddot{x} + b\dot{x} + kx$	$F_{c2} = m\ddot{x} + b\dot{x} + kx$	2.39	1.13	-0.71	5.76	6.47	172.64	71.77	0.66 (+37%)	1.44 (-13%)
2	$G_{c2} = m\ddot{x} + b\dot{x} + kx$	$F_{c1} = b\dot{x} + kx$	2.76	0.98	-0.02	5.94	5.97	196.53	57.97	0.82 (+71%)	1.87 (+12%)
3	$G_{c2} = m\ddot{x} + b\dot{x} + kx$	$F_{ch} = c\dot{x}$	3.82	0.31	2.35	4.97	2.62	182.10	70.68	0.75 (+56%)	1.93 (+15%)
4	$G_{c1} = b\dot{x} + kx$	$F_{c2} = m\ddot{x} + b\dot{x} + kx$	2.77	1.02	-0.08	6.22	6.31	192.31	58.25	0.80 (+66%)	1.78 (+6%)
5	$G_{c1} = b\dot{x} + kx$	$F_{c1} = b\dot{x} + kx$	2.64	1.02	-0.05	6.04	6.09	181.79	65.15	0.70 (+46%)	1.47 (-12%)
6	$G_{c1} = b\dot{x} + kx$	$F_{ch} = c\dot{x}$	3.80	0.31	2.31	4.89	2.58	198.31	54.83	0.83 (+73%)	2.04 (+22%)
7	$G_{c0} = 0$	$F_{c2} = m\ddot{x} + b\dot{x} + kx$	2.89	1.09	-0.05	6.76	6.81	160.48	75.55	0.58 (+21%)	1.78 (+6%)
8	$G_{c0} = 0$	$F_{c1} = b\dot{x} + kx$	2.83	1.05	-0.11	6.67	6.78	164.49	72.68	0.59 (+23%)	1.85 (+11%)
9	$G_{c0} = 0$	$F_{ch} = c\dot{x}$	3.84	0.29	2.41	5.06	2.65	170.66	72.84	0.62 (+29%)	2.08 (+24%)
10	$G_c = 0$	$F_c = 0$	2.13	1.55	-0.54	8.94	9.48	136.64	81.66	0.48 (0.0%)	1.68 (0.0%)

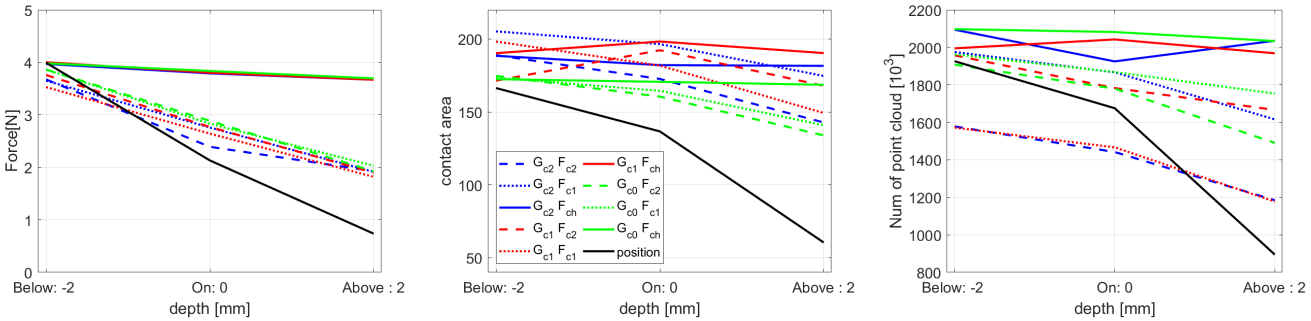

(A) (B) (C)

Fig. 6: Experimental results of robotic US scanning by using "Below", "On", and "Above" the surface trajectories: A) contact force, B) the length of segmented ligament, and C) the number of reconstructed pointclouds.

IV. DISCUSSION AND CONCLUSIONS

This paper aims to present a comprehensive comparison study on a semi-automatic robotic US scanning system that incorporates 3D US reconstruction. To accomplish this, the system implements multiple admittance-based controllers, which facilitate the robot's tracking of the reference trajectory while ensuring a consistent force in the direction perpendicular to the contact point.

The proposed automatic scanning system has two advantages in terms of applied force. First, the applied scanning force yields at 3.83 ± 0.31 N and is rather low than other similar works with 6.11 ± 1.18 N in previous research [20, 21]. Therefore it causes less tissue deformation in the patient, which may affect the diagnosis or interventions. For some tracking scenarios, the deformation is uniform over the skin, which causes fewer issues with surface tracking by depth camera [22]. Second, the admittance or impedance-based control scheme is used to interact with the environment; It needs to know the environment stiffness to have fast and stable behaviour, while the velocity admittance-based control scheme is able to reach constant contact force in the steady state without knowing the stiffness. It can scan and reconstruct other anatomies of the human body, such as soft or hard tissues, preserving large tissue deformation and allowing physicians to monitor the scanning process.

The US image quality with the proposed control strategies is also evaluated. It is assessed by evaluating the length of the segmented ligament from the phantom. Around 83% of the images contain a clear ligament with a layer length over 90%. The performance is stable when scanning over a complex shape surface with various depths. Consequently, the proposed velocity admittance-based control outperforms the position control and the admittance control. Intuitively, the quality of the US image and the probe performance were stable in the scanning process. The proposed evaluation approach cloud also be extended to the validation of US scanning on humans, since the contrast of soft tissue is better than on phantom. The length of the ligament layer and the area of the fat layer could be used to provide a quantitative assessment. Whereas, the evaluation criteria are also influenced by the segmentation approach. By training with more US images, the network could segment the ligament layer with a more accurate and precise boundary.

However, the proposed system has some limitations. Firstly, due to the collaboration path planning method, a user or sonographer is required to define the path. Therefore, an automatic path planning method can be added to this system to make it convenient, e.g. utilizing an RGBD camera to automatically detect scanning regions. The user-adjusted points may sometimes fall below the skin surface or extend into the air, resulting in invalid US image data. To mitigate these issues, it is imperative to implement a control mechanism for the US probe, enabling it to adapt its movement along the Z-axis with respect to the surface. This

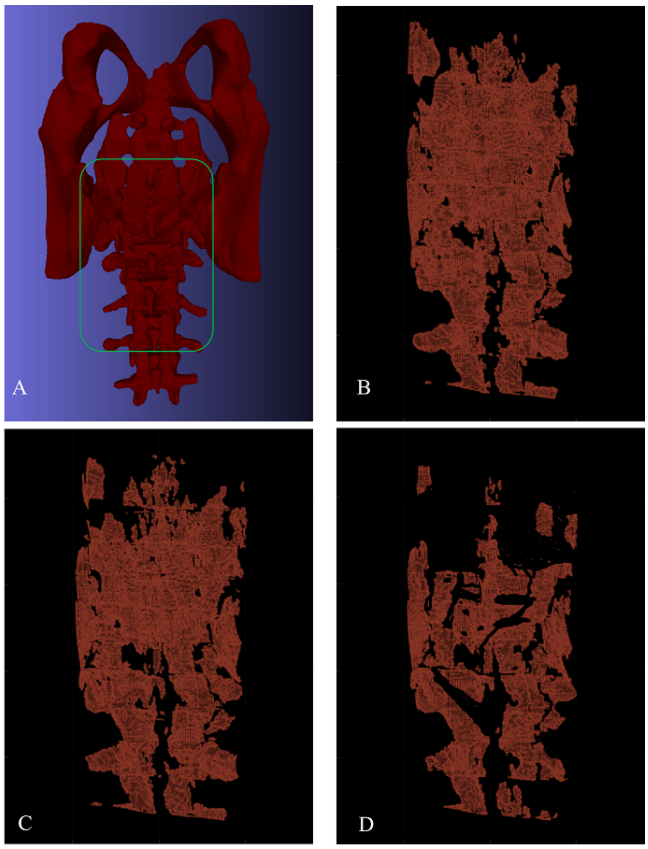

Fig. 7: A) CT model and the scanned area (in green block) on the CIRS phantom. Examples of 3D reconstruction for the proposed control strategies: B) velocity admittance control (Exp. 3), C) admittance control (Exp. 1), and D) position control (Exp. 10).

entails enabling the US probe to ascend or descend smoothly when encountering convex or concave surfaces. Secondly, this experiment has been conducted on the static phantom only without breathing motion. In contrast, real-world scenarios involving patients introduce physiological motions such as breathing and heartbeats. Addressing these motion-related challenges will be crucial for ensuring accurate and reliable imaging outcomes in clinical settings. By using an optical marker on the patient's back, the breathing motion could be monitored and predicted during the scanning.

Importantly, it is helpful to investigate and model the manual scanning from expert sonographers in the future. The recovery of the "language of sonography" [23] could be considered as valuable and essential as the progress made in the robotic US examination.

The proposed semi-automatic robotic US reconstruction has promising potential to be applied in clinical applications as a non-radiation imaging solution. This approach establishes a systematic approach for generating three-dimensional anatomical structures through a robot-assisted US system. The robotic US system guarantees precise hybrid admittance control by maintaining a constant force at a comparably low magnitude. The qualitative reconstruction outcomes demonstrate that the lumbar training phantom's geometric attributes can be accurately reconstructed while ensuring a consistent scanning force.

This study comprehensively assesses various control strategies implemented on a semi-automatic robotic US system. The control strategies under scrutiny encompass traditional position control, admittance control, and the velocity-based admittance control proposed in this research. The preliminary results pave the way for future clinical practice.

References

[1] J. Troccaz, G. Dagnino, and G.-Z. Yang. "Frontiers of Medical Robotics: From Concept to Systems to Clinical Translation". In: *Annu. Rev. Biomed. Eng.* 21 (2019), pp. 193–218.

[2] Marcel K Welleweerd et al. "Automated robotic breast ultrasound acquisition using ultrasound feedback". In: *presented at the 2020 IEEE International Conference on Robotics and Automation (ICRA)* (2020).

[3] Vincent Groenhuis et al. "3-D ultrasound elastography reconstruction using acoustically transparent pressure sensor on robotic arm". In: *IEEE Trans. Med. Robot. Bionics* 3.1 (2021), pp. 265–268.

[4] Chunwoo Kim et al. "Ultrasound probe and needle-guide calibration for robotic ultrasound scanning and needle targeting". In: *IEEE Trans. Biomed. Eng.* 60.6 (2013), pp. 1728–1734.

[5] Qianqian Cai et al. "Spatial calibration for 3D freehand ultrasound via independent general motions". In: *presented at the 2020 IEEE International Ultrasonics Symposium (IUS)* (2020).

[6] Zhongliang Jiang et al. "Automatic force-based probe positioning for precise robotic ultrasound acquisition". In: *IEEE Transactions on Industrial Electronics* (2020).

[7] Zhongliang Jiang et al. "Automatic normal positioning of robotic ultrasound probe based only on confidence map optimization and force measurement". In: *IEEE Robotics and Automation Letters* 5.2 (2020), pp. 1342–1349.

[8] Jay Carriere et al. "An admittance-controlled robotic assistant for semi-autonomous breast ultrasound scanning". In: *2019 international symposium on medical robotics (ISMR)*. IEEE. 2019, pp. 1–7.

[9] Ting-Yun Fang et al. "Force-assisted ultrasound imaging system through dual force sensing and admittance robot control". In: *International journal of computer assisted radiology and surgery* 12.6 (2017), pp. 983–991.

[10] Maria Victorova, David Navarro-Alarcon, and Yong-Ping Zheng. "3D ultrasound imaging of scoliosis with force-sensitive robotic scanning". In: (2019), pp. 262–265.

[11] R. Jia et al. "Automatic bone segmentation in ultrasound images using local phase features and dynamic programming". In: *Proc. Int. Symp. Biomed. Imaging* (2016), pp. 1005–1008.

[12] Pierre Chatelain, Alexandre Krupa, and Maud Marchal. "Real-time needle detection and tracking using a visually servoed 3D ultrasound probe". In: *2013 IEEE International Conference on Robotics and Automation*. IEEE. 2013, pp. 1676–1681.

[13] Qinghua Huang, Jiulong Lan, and Xuelong Li. "Robotic arm based automatic ultrasound scanning for three-dimensional imaging". In: *IEEE Transactions on Industrial Informatics* 15.2 (2018), pp. 1173–1182.

[14] Ruixuan Li et al. "Comparative quantitative analysis of robotic ultrasound image calibration methods". In: *2021 20th international conference on advanced robotics (ICAR)*. IEEE. 2021, pp. 511–516.

[15] Ruixuan Li, Kenan Niu, and Emmanuel Vander Poorten. "A Framework for Fast Automatic Robot Ultrasound Calibration". In: *2021 International Symposium on Medical Robotics (ISMR)* (2021), pp. 1–7. DOI: 10.1109/ismr48346.2021.9661495.

[16] Marie Schumacher et al. "An introductory review of active compliant control". In: *Robotics and Autonomous Systems* 119 (2019), pp. 185–200.

[17] Jonathan J Kaufman and Thomas A Einhorn. "Perspectives: Ultrasound assessment of bone". In: *Journal of Bone and Mineral Research* 8.5 (1993), pp. 517–525.

[18] Olaf Ronneberger, Philipp Fischer, and Thomas Brox. "U-Net: Convolutional Networks for Biomedical Image Segmentation". In: *Lecture Notes in Computer Science*. 9351 (2015), pp. 234–241. DOI: 10.1007/978-3-319-24574-4_28.

[19] Ruixuan Li et al. "Robot-assisted ultrasound reconstruction for spine surgery: from bench-top to pre-clinical study". In: *International journal of computer assisted radiology and surgery* (2023), pp. 1–11.

[20] Filip Suligoj et al. "RobUSt–An Autonomous Robotic Ultrasound System for Medical Imaging". In: *IEEE Access* 9 (2021), pp. 67456–67465.

[21] Guochen Ning et al. "Force-guided autonomous robotic ultrasound scanning control method for soft uncertain environment". In: *International Journal of Computer Assisted Radiology and Surgery* (2021), pp. 1–11.

[22] Qinghua Huang et al. "Fully automatic three-dimensional ultrasound imaging based on conventional B-scan". In: *IEEE transactions on biomedical circuits and systems* 12.2 (2018), pp. 426–436.

[23] Zhongliang Jiang, Septimiu E. Salcudean, and Nassir Navab. "Robotic ultrasound imaging: State-of-the-art and future perspectives". In: *Medical Image Analysis* (2023), p. 102878.